RAA 2016 Vol. **16** No. **1**, 5 (12pp) doi: 10.1088/1674–4527/16/1/005
http://www.raa-journal.org *http://iopscience.iop.org/raa*

Research in Astronomy and Astrophysics

Solar flares with similar soft but different hard X-ray emissions: case and statistical studies

Ivan N. Sharykin[1], Alexei B. Struminsky[1], Ivan V. Zimovets[1] and Wei-Qun Gan[2]

[1] Space Research Institute, Russian Academy of Sciences, Moscow 117997, Russia; *ivan.sharykin@phystech.edu*

[2] Purple Mountain Observatory, Chinese Academy of Sciences, Nanjing 210008, China

Received 2014 December 29; accepted 2015 July 1

Abstract From the *Reuven Ramaty High Energy Solar Spectroscopic Imager* (*RHESSI*) catalog we select events which have approximately the same *GOES* class (high C - low M or 500–1200 counts s^{-1} within the *RHESSI* 6–12 keV energy band), but with different maximal energies of detected hard X-rays. The selected events are subdivided into two groups: (1) flares with X-ray emissions observed by *RHESSI* up to only 50 keV and (2) flares with hard X-ray emission observed also above 50 keV. The main task is to understand observational peculiarities of these two flare groups. We use *RHESSI* X-ray data to obtain spectral and spatial information in order to find differences between selected groups. Spectra and images are analyzed in detail for six events (case study). For a larger number of samples (85 and 28 flares in the low-energy and high-energy groups respectively) we only make some generalizations. In spectral analysis we use the thick-target model for hard X-ray emission and one temperature assumption for thermal soft X-ray emission. *RHESSI* X-ray images are used for determination of flare region sizes. Although thermal and spatial properties of these two groups of flares are not easily distinguishable, power law indices of hard X-rays show significant differences. Events from the high-energy group generally have a harder spectrum. Therefore, the efficiency of chromospheric evaporation is not sensitive to the hardness of nonthermal electron spectra but rather depends on the total energy flux of nonthermal electrons.

Key words: Sun: flares — Sun: X-rays — gamma rays

1 INTRODUCTION

Solar flares involve highly sophisticated processes, such as particle acceleration (revealed by nonthermal hard X-ray (HXR) and radio emissions), plasma heating up to extremely high temperatures (observed as soft X-ray (SXR) emissions), and plasma motions with velocities up to supersonic and super-Alfvénic values. A large variety of flares are observed due to the complexity of the magnetic field topology and the irregularity of the plasma properties. One of the characteristics of a flare is an intensity peak observed within the 1–8 Å band - the X-ray flare importance which is determined by the X-ray detectors on the *Geostationary Operational Environmental Satellite* (*GOES*). However, flares of the same *GOES* importance could have different HXR intensities and spectral properties.

In the previous studies related to statistics of parameters of flare HXR and SXR emissions, the authors usually determined the distribution of physical parameters connected with accelerated particles (Bromund et al. 1995; Saint-Hilaire et al. 2008; Krucker & Lin 2008; Xu et al. 2008; Hannah et al. 2011; Emslie et al. 2012; Guo et al. 2013) and heated plasma (Ryan et al. 2012; Li et al. 2012). Battaglia et al. (2005) provided evidence for the correlation between HXR flux at 35 keV and SXR flux. Veronig et al. (2002) showed a positive correlation between HXR and SXR fluxes: hotter flares with more intensive thermal X-ray emissions need more nonthermal electrons for plasma heating. Such a general relation between HXR and SXR emissions is called the Neupert effect (Neupert 1968), which assumes heating of chromospheric plasma is due to non-thermal energy input and subsequent chromospheric evaporation (plasma flows into the corona from the overheated chromosphere). However, flares with a very different/similar HXR spectrum but similar/different SXR intensities are often observed. Zimovets & Struminsky (2012) showed an example of the event on 2003 October 26, when two subsequent (with a 90 minute delay) HXR bursts with similar intensities resulted in very different SXR emissions. This was explained by chromospheric plasma that evaporated into magnetic loops with different spatial scales in the impulsive and decay phases. It is also worth noting that some observations show flares with distinguishable thermal emissions but moderate HXR intensities (Sharykin et al. 2015).

We start our studies from the comparison of two flares, which had approximately the same *GOES* importance and occurred in the same active region, but which were separated in time by one day (Fig. 1). The flare from 2002

February 25 had HXR emissions up to 50 keV, while the event of 2002 February 26 showed gamma-ray emissions up to $\sim$1 MeV. The *RHESSI* count rate within the 25–50 keV energy band was about one order of magnitude lower in the first event than in the second one.

McDonald et al. (1999) investigated several flares with high HXR fluxes but unusually weak SXR emissions and compared them with "normal" flares which have increasing HXRs accompanied by increasing SXRs described by the Neupert effect. Such difference was explained by different energy fractions of nonthermal electrons related to chromospheric evaporation. Based on this idea, we carry out a statistical analysis with better spectral and spatial resolutions of *RHESSI* observations and we select flares according to their maximal HXR energies detected. Veronig et al. (2002) and Hannah et al. (2008) also showed the absence of a correlation between SXR fluxes (thermal energy) and HXR power-law index, i.e., chromospheric evaporation is not always related to the hardness of the nonthermal electron spectrum. In our work we will search for differences between flares with similar peak SXR fluxes, but a different HXR spectrum (during the time of HXR peak). The aim of this paper is to investigate the influence (or its absence) of hardness of the non-thermal electron spectrum on the thermal response of solar flare plasma observed in the range of SXR emission.

In this paper we consider events which are similar to the flares on 2002 February 25 and February 26. First we will analyze six flares in detail and then we will do a statistical survey of a larger number of the flares. This article is divided into the following sections: Section 2 data, instrumentation and event selection, Section 3 spectral analysis of *RHESSI* data, Section 4 statistical analysis of *GOES* data, Section 5 *RHESSI* X-ray imaging, and Section 6 discussion and conclusions.

2 DATA, INSTRUMENTATION AND EVENT SELECTION

We use data from the *RHESSI* spacecraft providing us with X-ray light curves, spectra and images in the energy range of 3–17000 keV (Lin et al. 2002). The *RHESSI* spectrometer was described by Smith et al. (2002) and the *RHESSI* imaging technique was presented in Hurford et al. (2002). Reconstruction of *RHESSI* spectra and images is made using the *RHESSI* package and the OSPEX package within SolarSoftWare (SSW).

Processing time series of *RHESSI* spectra for a large number of flares is a very complicated task as we have to select the precise fitting model and understand all peculiarities of particular events. To simplify this, we use the rise phase of the *GOES* SXR data to obtain the integrated radiated energy of flares. The SXR detectors aboard *GOES* include observations in two channels, which allow us to estimate the temperature and emission measurements of flare plasma (Thomas et al. 1985).

Solar flares of C-M *GOES* classes are selected from the *RHESSI* catalog from 2002 until 2009 (within the 23rd solar cycle) using the *RHESSI*_flare_obj in the *RHESSI* package according to the following criteria:

(1) Peak values of the *RHESSI* count rates in the 6–12 keV band must be within the range of 500–1200 counts s^{-1}. The lower limit is set to guarantee counting statistics while the higher one is selected to avoid the pulse pile up effect.
(2) Attenuator state must be 1 (the thin shutter) during the HXR peaks. It is necessary to have energies larger than 6 keV for spectral analysis and to avoid pile ups.
(3) Flare positions according to the *RHESSI* catalog must be below 940″ from the center of the Sun. It is necessary to avoid occulted flares in our sample as we are interested in HXR emissions from the flare footpoints. The value 940″ corresponds to the angular size of the Sun's radius when Earth is at aphelion.
(4) Quality of the *RHESSI* data must be good for analysis, i.e., the considered time intervals must not overlap with time periods when the spacecraft flys through the South Atlantic Anomaly (SAA), spacecraft night times, data gaps, particle events and so on.

In total, 113 events were selected for statistical analysis. These flares are divided into two groups: (1) flares with HXR emissions less than 50 keV (the low-energy group, 85 events), and (2) flares with HXR emission more than 50 keV (the high-energy group, 28 events). The 50 keV boundary is empirically selected to divide flares into soft and hard events.

For a detailed study, we selected a few particular events with similar SXRs but different HXRs. Six events (three from each group), which are summarized in Table 1, are selected manually for a case study. In these flares we can easily determine the preflare background in the whole energy range. Observations of these events have also avoided *RHESSI* attenuator changes. However, we allow the attenuator to change between states 0 and 1 in the statistical analysis.

3 SPECTRAL ANALYSIS OF *RHESSI* DATA

3.1 Case Study

We accumulate spectra in the energy range of 3–250 keV in 20 s intervals during HXR peaks of the highest available energy band. We use the sum of the counts from detectors 1, 3–6, 8 and 9 in order to increase the signal-to-noise ratio. The X-ray spectra are fitted by means of the least squares method. We consider spectra of the selected events to be a combination of thermal and nonthermal components. We use an isothermal model to fit the thermal part of the X-ray spectra, and a thick-target model (Brown 1971) for the nonthermal part. The pileup_mod method is applied for accounting for pile up effects in count spectra.

The energy range of 6–60 keV is used for spectral analysis of events from the low-energy group while the energy range is 6–250 keV for the high-energy group. Spectra

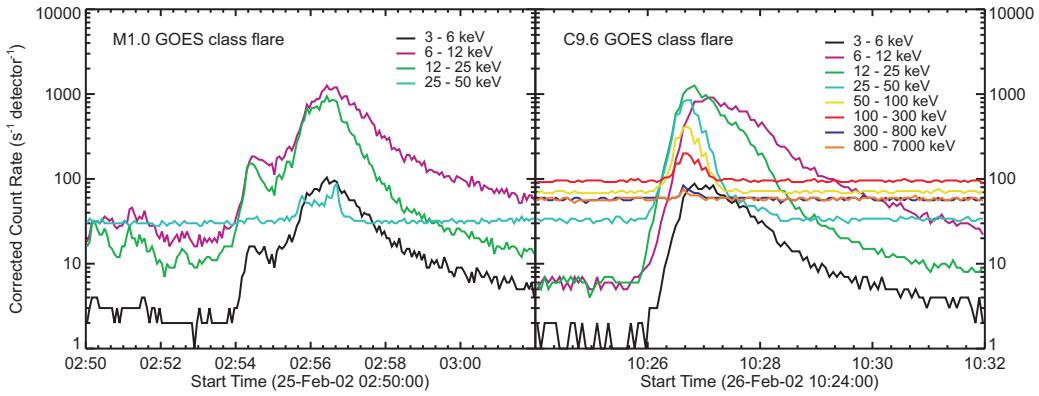

Fig. 1 Comparison of the *RHESSI* count rates in two solar flares from 2002 February 25 (*left*) and 2002 February 26 (*right*).

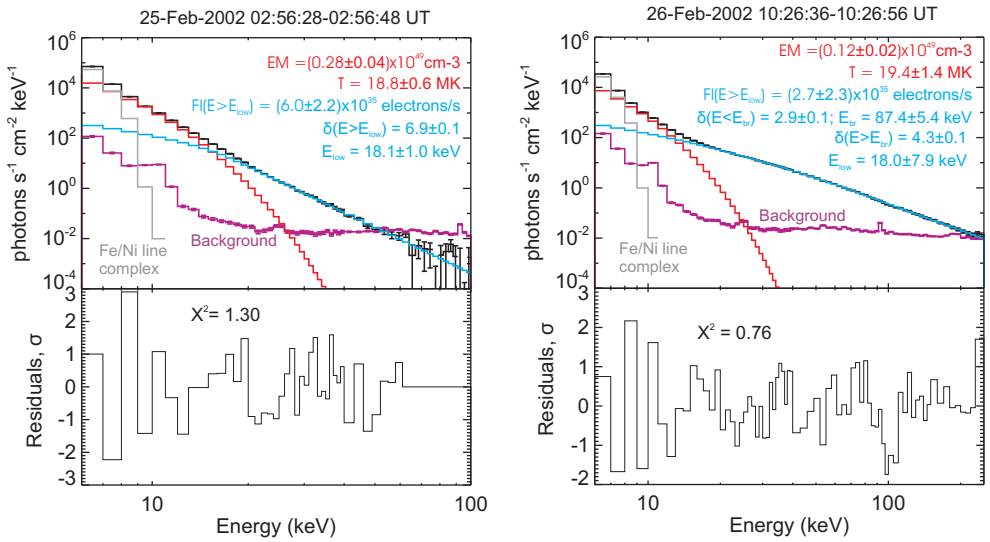

Fig. 2 Fitting results of the *RHESSI* X-ray spectra of the 25–Feb–2002 M1.0 flare (*left panel*) and 26–Feb–2002 C9.6 flare (*right panel*). Black line - *RHESSI* spectral data with background (violet) subtracted, red line - isothermal model, and blue line - thick-target model with a single power law approximation to the nonthermal electron spectrum in the left panel and a broken power law approximation to the nonthermal electron spectrum in the right panel. Histograms below the spectra are residuals of the fittings.

of nonthermal electrons in the low-energy group are assumed to have the form of a single power law with a low-energy cutoff. However, for the high-energy group we use a double power law approximation, as the single power law approximation with low-energy cutoff leads to a worse fitting in some cases.

Line emissions from the Fe/Ni complex (centroids at 6.5 and 8 keV) have been taken into account for obtaining good fits in the energy range of 6–10 keV. An isothermal model of the continuum and line emission in X-rays is based on the CHIANTI data base (Dere et al. 2009), where Fe/Ni abundance ratio is a free parameter in the least squares method and abundances of other ions are fixed to coronal values.

The low-energy cutoff (Kontar et al. 2008; Hannah et al. 2009; Guo et al. 2011) of the nonthermal electron spectrum is a free parameter to improve linkage between thermal and nonthermal parts of the X-ray spectrum. Different flares have different thermal-nonthermal transitions and the low-energy cutoffs of the nonthermal part are not necessarily the same (e.g., Gan et al. 2001). Therefore, we use the low-energy cutoff as a free parameter during the spectral fitting.

Finally, we have six free parameters in the least squares method for the low-energy group: T - temperature, EM- emission measure, Fe/Ni line intensity, Fl - total flux of nonthermal electrons, and δ - their power law index and low-energy cutoff of nonthermal electron spectrum $E_{\rm low}$. For the high-energy group we have eight free parameters: T, EM, Fe/Ni line intensity, Fl, $E_{\rm low}$ and $E_{\rm break}$ - break energy that separates the two power law parts with corresponding spectral indices δ_1 ($E < E_{\rm break}$) and δ_2 ($E > E_{\rm break}$). Figure 2 shows examples of the fitted photon spectra for the two events presented in Figure 1.

The fitting results for six events selected for the case study are presented in Table 1, where values for δ_1 are shown as δ. We do not present $E_{\rm break}$ for the events from the high-energy group, since they have values above 100 keV and the nonthermal electron flux is mostly determined by electrons below $E_{\rm break}$. It is apparent that we have much steeper nonthermal electron spectra (6.9–7.5) for the low-energy group than for the high-energy group (2.9–3.7). The low-energy group is characterized by $\sim$2–3 times larger total fluxes of nonthermal electrons than those for the flares from the high-energy group. However one can see that the considered events have slightly different *GOES* classes. For more details concerning the relationship between different fluxes of nonthermal electrons and SXR emission response in the studied six flares, see the section entitled "Discussion."

3.2 Statistical Analysis

Here we apply the same model for X-ray spectral fitting as in the case study. Time intervals for accumulation of the background are taken from the *RHESSI* catalog. For energies higher than 25 keV, X-ray background is calculated from real *RHESSI* count rates. Below 25 keV we simulated the background using the SSW procedure hsi_spec_bck.pro, which uses longitude and latitude of the *RHESSI* spacecraft as input data to estimate a background spectrum. Fittings of 85 events from the low-energy group and 28 events from the high-energy group provide distributions of full chi-square values (Fig. 3-A and D). In the following analysis we only take into account the spectra fitted with $\chi^2 < 3\sigma$, i.e., 72 events from the low-energy group and 22 events from the high-energy group.

Fitting of HXR spectra of the events from the low-energy group gives us a mean value of 5.8 (Fig. 3-B) for the spectral power law index (δ) of nonthermal electrons, while for the high-energy group the spectral index has a mean value of about $\delta_1 \approx 3.9$ (Fig. 3-E). The difference between spectral indices of these two groups is significant. In this paper we do not discuss physics of the break energies E_{br} in the spectra of nonthermal electrons as it is out of the scope of this work.

Figure 4 shows histograms of temperature, emission measure, and Fe/Ni abundance distributions obtained from fitting the *RHESSI* spectra. Average values and dispersions are marked in the plots. It is shown that distributions for both samples are quite similar to each other in terms of shapes, peaks and mean values. Therefore the two flare groups show very similar thermal properties.

In Figure 3-C and F we present the values of the low-energy cutoffs of nonthermal electrons spectra obtained from fittings of the HXR spectra. One can note that the largest fraction of the studied flares has the values of low-energy cutoffs distributed within the energy range of 10–25 keV. The most frequent value of the low-energy cutoff is ≈ 12 keV.

4 STATISTICAL ANALYSIS OF *GOES* DATA

To make some estimations of the energetics and SXR rise times of the selected flares we will use the *GOES* data. For statistical analysis it is much better to use the *GOES* data as they cover all flare duration and the *GOES* background is only associated with SXR emission of the solar active regions and is not strongly affected by the surrounding medium. In this context, *RHESSI* is not a good instrument due to high variability of the background and the data gaps associated with the SAA, solar eclipses and particle events.

The *GOES* detectors observe SXR emissions in two channels: 0.5–4 Å and 1–8 Å. Temperature and emission measure can be evaluated from registered SXR fluxes in these channels (Thomas et al. 1985). A background level is assumed to be 95% of the minimal value of SXR flux registered during the preflare or postflare times. A selected 95% fraction of this flux accounts for an arbitrary presence of quiescent emission from the preflare region. This approach is a simplified variant of a technique used in the work by Ryan et al. (2012) and allows us to avoid unnatural temporal behavior of emission measure and temperature.

To estimate the rise time we use start and peak times defined in the *GOES* catalog. In order to include a solar flare in the *GOES* catalog, the flare must follow two criteria: (1) there must be a continuous increase in the one-minute averaged SXR flux in the 1–8 Å channel for the first four minutes of the event; (2) the flux in the fourth minute must be at least 1.4 times the initial flux. The start time of the event is defined as the first of these four minutes.

Distributions of the maximal SXR fluxes in two *GOES* channels (Fig. 5-A and B) for both groups of flares show that the average magnitude of the *GOES* class of a high-energy flare is twice as large as the *GOES* class of a low-energy flare. Distributions of the rise times (Fig. 5-C, rise time is the difference between peak and start time in the 1–8 Å channel) do not show clear differences between the two groups. Derived maximal temperature and emission measure are presented in Figures 5-D and E respectively and we also see that both groups of flares have similar temperature distributions, but the average maximal emission measure of the high-energy group is 30% larger than the average emission measure of the low-energy group. Total radiated energy (integrated over the whole time of the flare duration) is presented in Figure 5-F. We see a difference by a factor of $\sim$0.7 between the average total energy radiated in the SXR range during flares from the low-energy and high-energy groups, which are respectively $\approx 6.8 \times 10^{29}$ and 9.6×10^{29} erg.

5 *RHESSI* X-RAY IMAGING

From the previous sections we deduced the temperature and emission measure distributions for the events from our two groups. In order to estimate the plasma density, which is about $\sqrt{EM/V}$, we need to estimate the approximate volume of the flare regions emitting SXRs.

Table 1 The results of X-ray spectral fitting for events selected for case study analysis. UT time corresponds to the center of the 20-second time interval used for obtaining the spectra.

Event date and UT	*GOES* class	T (MK)	EM (10^{49} cm^{-3})	$Fl(E > E_{\rm low}$ keV) (10^{35} s^{-1})	δ	$E_{\rm low}$ (keV)	χ^2 σ
25–Feb–2002, 02:56:40	M1.0	18.8±0.6	0.28±0.04	6.0±2.2	6.9±0.1	18.1±1.0	1.3
16–Apr–2002, 13:10:50	M2.5	19.3±0.7	0.35±0.06	8.6±2.3	7.3±0.1	19.1±0.7	0.9
11–Jul–2002, 14:17:55	M1.0	20.0±0.7	0.13±0.02	3.2±0.7	7.5±0.1	20.4±0.6	1.5
26–Feb–2002, 10:26:45	C9.6	19.4±1.4	0.12±0.02	2.7±2.3	2.9±0.1	18.0±7.9	0.74
28–Aug–2002, 10:59:30	C9.3	26.2±1.0	0.03±0.01	1.4±1.0	3.7±0.1	20.4±4.7	1.55
6–May–2005, 03:08:40	C5.7	22.0±3.8	0.02±0.01	2.0±0.3	3.6±0.1	19.8±5.7	0.99

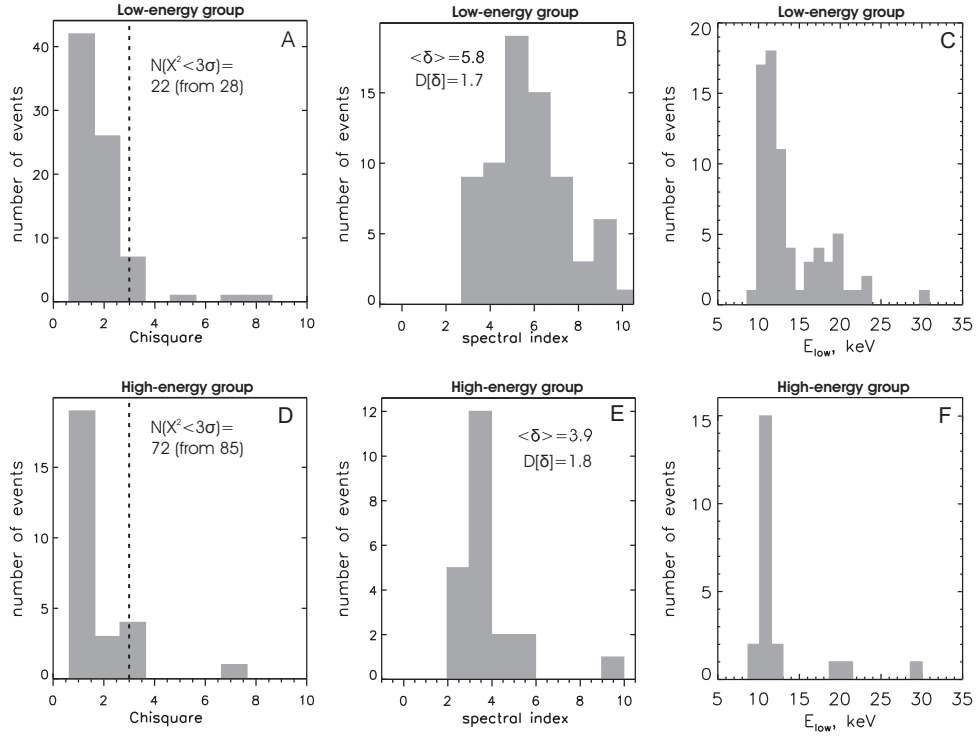

Fig. 3 The upper and lower three panels show results of spectral fittings for the low-energy and high-energy groups respectively. Panels (A) and (D) present histograms of χ^2 of *RHESSI* spectral fittings; (B) and (E) show distributions of spectral indices δ of nonthermal electron spectra; (C) and (F) show distributions of low-energy cutoffs $E_{\rm low}$ of nonthermal electron spectra. The mean values and dispersions of the distributions are written within the corresponding panels.

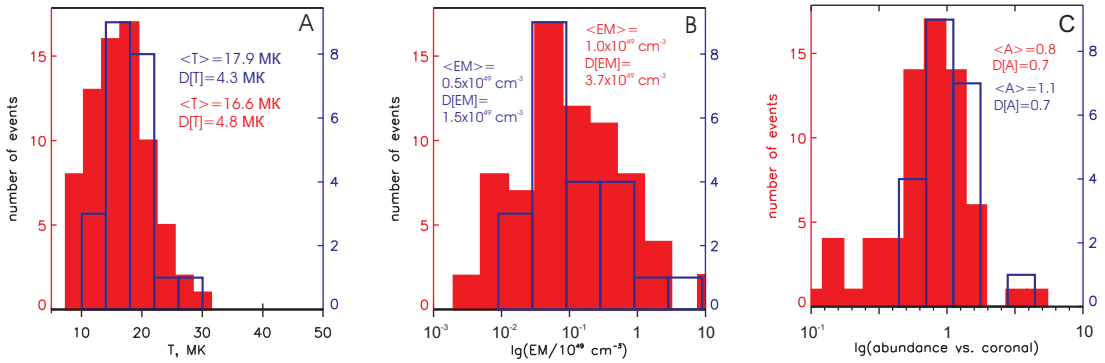

Fig. 4 A - temperature; B - emission measures; C - ratio of the abundance of Fe and Ni ions based on the coronal CHIANTI model. Red and blue colors mark the low-energy and the high-energy groups respectively. The mean values and dispersions of the distributions are written within the corresponding panels. *RHESSI* spectra are analyzed during 20 seconds around HXR peaks of the flares.

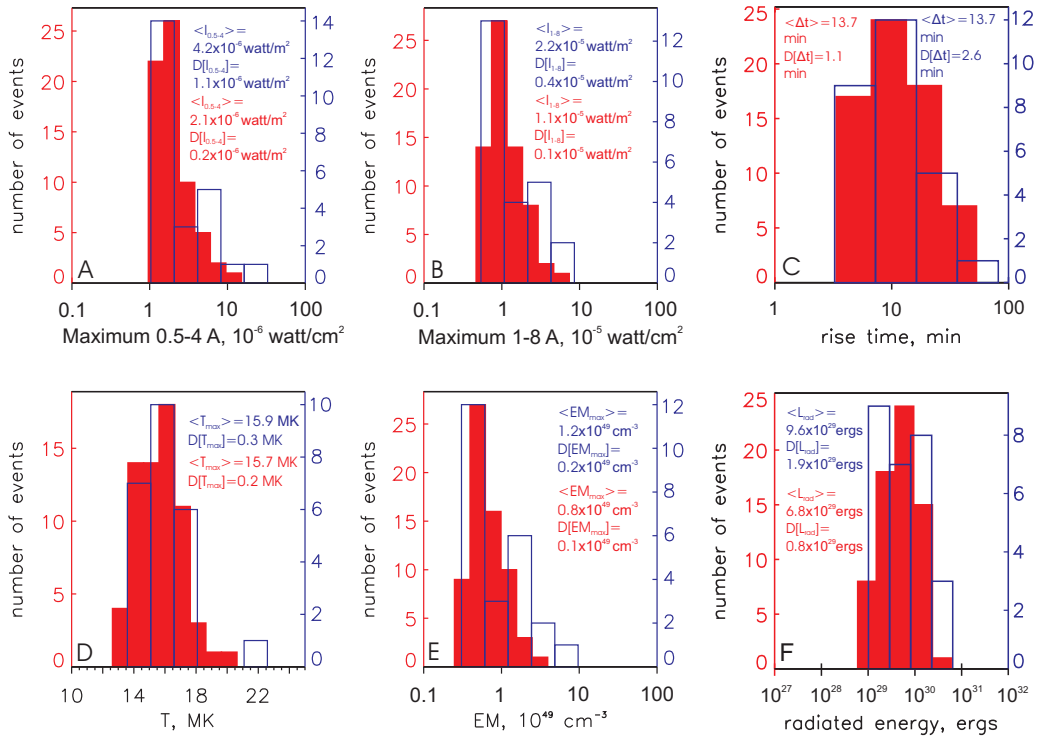

Fig. 5 Panels A and B show distributions of maximal intensities within shortwave (0.5–4 Å) and longwave (0.5–4 Å) *GOES* channels respectively; C - rise time; D and E present distributions of maximal temperature and emission measure of the flares respectively; F shows the total radiated energy in the SXR range. Red and blue colors mark the low-energy and the high-energy group respectively; the mean values and dispersions of the distributions are written within the corresponding panels.

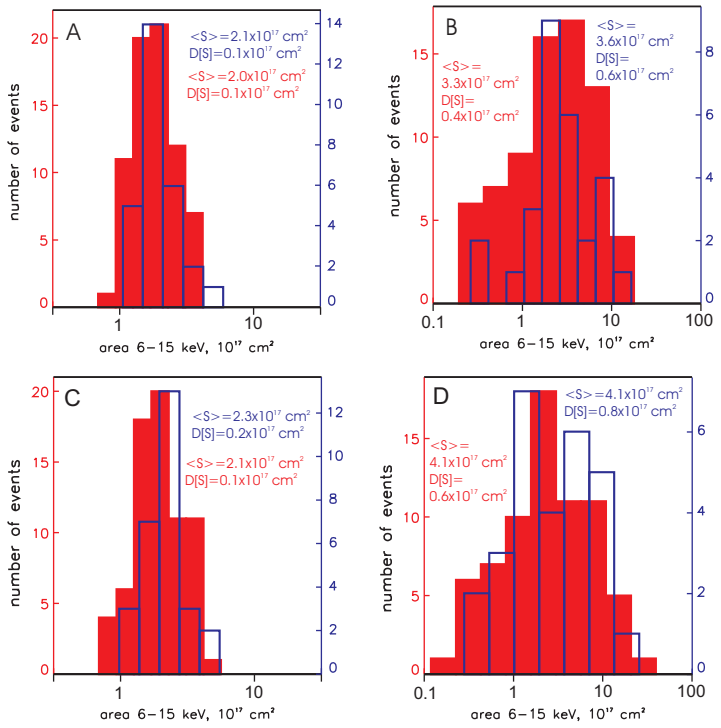

Fig. 6 Upper panels A and B show distributions of areas of 6–15 keV X-ray sources, obtained by CLEAN with uniform weighting; lower panels C and D show the same as the upper panels but using CLEAN with natural weighting; A and C - X-ray sources are estimated by assuming an elliptical Gaussian shape; B and D - X-ray sources are assumed to have circular shapes; red - the low-energy group, blue - the high-energy group; the mean values and dispersions of the distributions are written within the corresponding panels.

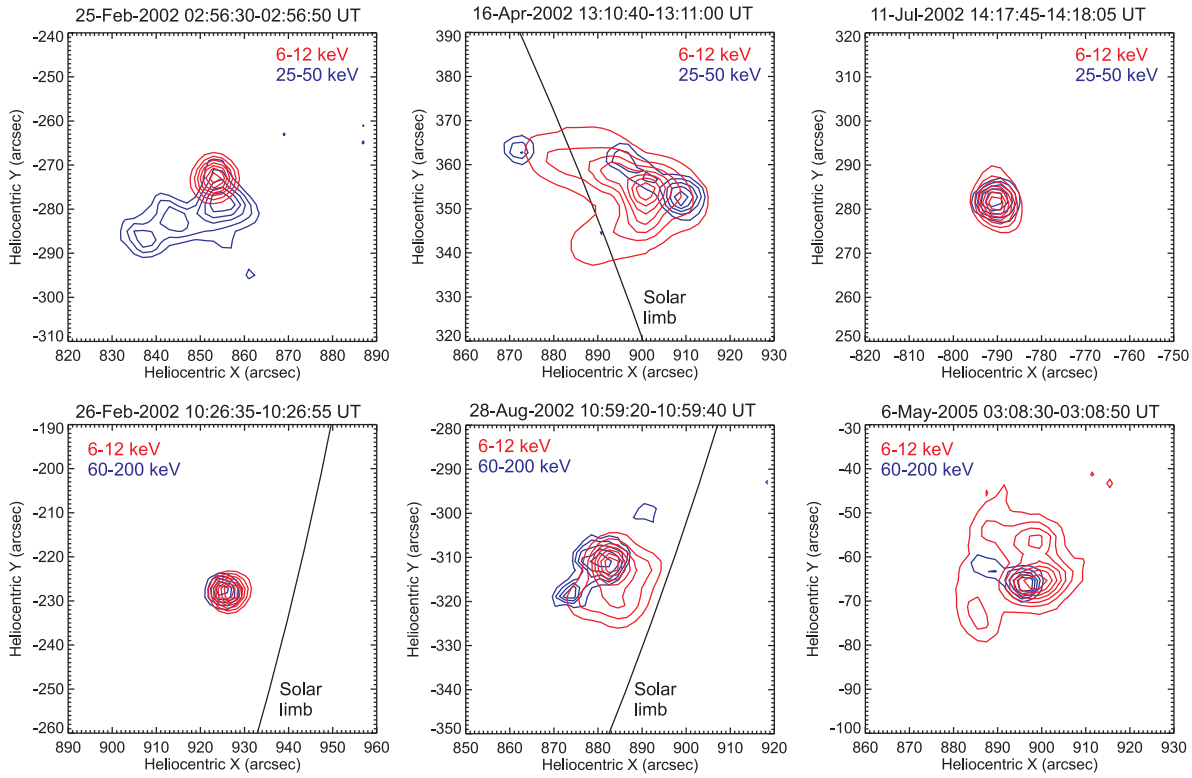

Fig. 7 CLEAN images with natural weighting made for the six events listed in Table 1. The upper three panels show flares from the low-energy group, while the lower three panels present flares from the high-energy group.

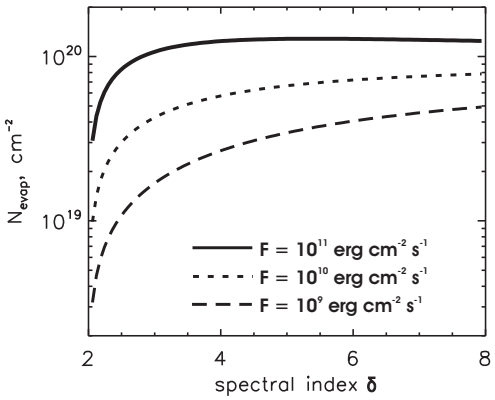

Fig. 8 Analytic calculations of $N_{\rm evap}$ according to Equation (1).

The *RHESSI* software package contains several algorithms for obtaining images. Dennis & Pernak (2009) discussed advantages and disadvantages of these methods. Here we use the CLEAN algorithm with both types of weighting of the Fourier components: natural (Fig. 6-A and B) and uniform (Fig. 6-C and D). The first one is sensitive to diffuse sources, while the second is more appropriate for fine structured X-ray sources. Since we do not know details of X-ray sources, such as their shapes and sizes, we use both methods and search for differences between images obtained from the two groups.

The CLEAN algorithm often overestimates geometric parameters due to convolution of the real X-ray source with a Point Spread Function (PSF) averaged through the detectors that are used (3–6). So, a real linear scale of the source can be estimated as $R_{\rm real} = \sqrt{R_{\rm im}^2 - R_{\rm PSF}^2}$, where $R_{\rm real}$ is the full width at half maximum (FWHM) of the real source, $R_{\rm im}$ is the measured FWHM and $R_{\rm PSF}$ is the PSF FWHM. We use two techniques to estimate the linear scale of an X-ray source: (1) $R_{\rm im}$ is a radius of the circle with area $\pi R_{\rm im}^2$ equal to the area of the X-ray source limited by a 50% contour; (2) a and b are the major and minor axes

respectively of an elliptical Gaussian with area πab, used for fitting the X-ray source. Values of $R_{\rm im}$, a and b are corrected by accounting for the convolution with PSF. Images are reconstructed for all studied flares requiring a signal-to-noise ratio in the brightest pixel > 3 (according to Poisson statistics): 72 out of 85 from the low-energy group and all events (28) from the high-energy group are selected. Distributions of areas $S_{\rm SXR}$ of 6–15 keV X-ray sources are summarized in Figure 6. This energy range mostly corresponds to thermal emissions.

Events from both groups have approximately similar distributions of X-ray source sizes. The ratio of average area values for the two groups is near unity. Linear dimensions $\sim S_{\rm SXR}^{1/2}$ and volumes $\sim S_{\rm SXR}^{3/2}$ of flares from both groups are also comparable to each other when accounting for the resolution capabilities of *RHESSI*.

In Figure 7 we present contour plots of X-ray *RHESSI* images for six events listed in the Table 1. These X-ray images are also synthesized by the CLEAN algorithm with natural weighting. One can see that we do not observe significant peculiarities for these low-energy and high-energy flares. We observe compact and extended sources for both groups of flares. Using 50% HXR contours in the energy range of 25–50 keV for the low-energy flares and a range of 60–200 keV for the high-energy flares, we can estimate the image plane cross sectional area of flare magnetic structures where we have precipitating nonthermal electrons. For the 16-Apr-2002 flare we observe a loop structure above the limb with a 25–50 keV coronal HXR source. To estimate the cross sectional area for this flare we use the footpoint HXR sources. Results of our estimations of $S_{\rm HXR}$ are shown in Table 2. In this table we also show PSF corrected $S_{\rm HXR}$, as described above. Results listed in Table 2 will be used for determination of nonthermal energy fluxes for the six flares that are studied.

6 DISCUSSION

The statistical and case study analysis presented above shows that events from the two groups are very similar in terms of temperature, emission measure, SXR intensity, integral SXR radiance, flare region size and SXR rise time. The most discernible difference is that between the HXR spectral indices, which indicates different slopes of the nonthermal electrons spectra. Accelerated electrons with different spectra lead to similar thermal feedback. Numerical simulations of gas dynamics and kinetics of accelerated particles could be carried out in order to investigate this problem analytically. Alternatively, we provide some simple explanations as follows.

We consider the energy of nonthermal electrons as a main source of plasma heating and radiative cooling. The chromospheric evaporation can be stimulated directly by precipitating nonthermal electrons, which overheat the chromosphere, or by heat transfer from the corona, which also might be heated by nonthermal electrons. In both scenarios, nonthermal electrons are responsible for the energy of the evaporated plasma. To estimate the fraction of nonthermal electron energy, which is deposited to the chromospheric evaporation, we use an approach described by McDonald et al. (1999).

The solar atmosphere is continuously heated by precipitating nonthermal electrons during solar flares; when the radiative losses of background plasma are too strong, the heating by nonthermal electrons is no longer efficient. Consider the specific energy loss rate due to radiation as $(n_i + n_n)f(T)$ for $f(T) = 7 \times 10^{-22}$ [erg cm^3 s^{-1}], for $T \sim 10^5$ K, where n_i and n_n are ion and neutral atom number densities respectively. We can expect that at some height above the photosphere all nonthermal electron energy would be radiated away, due to the large collisional rate which is proportional to n^2 in the dense part of the solar atmosphere. To estimate column density of plasma generated due to chromospheric evaporation, one can use the formula from (Veronig & Brown 2004)

$$N_{\rm evap}[{\rm cm}^{-2}] \approx 8.2\times10^{19}\Big[7.7\times10^{-12}B\Big(\frac{\delta}{2},\frac{1}{3}\Big)(\delta-2)\frac{P_{\rm nth}(E>E_{\rm low})}{S}p\Big]^{\frac{2}{\delta+2}}, \quad (1)$$

where $P_{\rm nth}(E > E_{\rm low}) = (\delta-1)/(\delta-2)Fl \cdot E_{\rm low}$ is kinetic power of nonthermal electrons with flux Fl for energies higher than the value of low-energy cutoff $E_{\rm low}$ of the nonthermal electron spectrum, S is the cross section of flare loop with length L, and p is correction for loop top pressure and considered here to be the same, ~ 1, in both groups of flares.

In Figure 7 we show that $N_{\rm evap}$ for different energy fluxes $F = P_{\rm nth}/S$ does not vary significantly for $\delta > 3$. However, the value of $N_{\rm evap}$ strongly depends on the energy flux of the nonthermal electrons.

It is reasonable to assume that energy input of nonthermal electrons to plasma is only determined by the integrated heating rate in the loop above this critical height $N_{\rm evap}$ (Fisher 1989)

$$\begin{aligned} F_{\rm evap} &= \Big[1-\frac{1}{3}B\Big(\frac{\delta}{2},\frac{1}{3}\Big)\Big[\frac{N_{\rm evap}}{N_{\rm low}}\Big]^{1-\frac{\delta}{2}}\Big]\cdot F\,, \\ &\quad \text{for } N_{\rm evap}\geq N_{\rm low} \\ F_{\rm evap} &= \Big[1-\frac{1}{3}B_{\frac{N_{\rm evap}}{N_{\rm low}}}\Big(\frac{\delta}{2},\frac{1}{3}\Big)\Big[\frac{N_{\rm evap}}{N_{\rm low}}\Big]^{1-\frac{\delta}{2}} \\ &\quad -\Big(1-\frac{N_{\rm evap}}{N_{\rm low}}\Big)^{\frac{1}{3}}\Big]\cdot F, \text{ for } N_{\rm evap}<N_{\rm low} \quad (2) \end{aligned}$$

where $B(x, y)$ is the beta function and $B_z(x, y)$ is the incomplete beta function; $N_{\rm evap}$ is the column depth along the magnetic loop derived from Equation (1), where the direct heating by nonthermal electrons is balanced by radiative cooling from the chromosphere; $N_{\rm low}$ is the column depth required to stop an electron with energy equal to the value of the low-energy cutoff $E_{\rm low}$. The value of $N_{\rm low}$ is estimated as $E_{\rm low}^2/3C$, where $C \approx 3.64 \times 10^{-18}$ keV ^{2} cm^2 (Fisher et al. 1985). We present the calculations of the $F_{\rm evap}/F$ for different δ and $E_{\rm low} <$

Table 2 Estimations of Areas of HXR Sources Using 50%-level Contours

Event	25–Feb–2002	16–Apr–2002	11–Jul–2002	26–Feb–2002	28–Aug–2002	6–May–2005
$S_{\rm HXR}$, arcsec^2	∼300	∼150	∼100	∼60	∼150	∼100
PSF corrected $S_{\rm HXR}$, arcsec^2	∼270	∼120	∼70	∼30	∼120	∼70

$\sqrt{3CN_{\rm evap}}$ in Figure 9-A and B. One can see a small difference between $F_{\rm evap}/F$ for $\delta > 3$, especially for $E_{\rm low} = 15$ keV. Thus, chromospheric evaporation energetics of high-energy flares and low-energy flares do not differ from each other significantly, considering similar values of F, since spectral indices (δ) of nonthermal electrons in them are larger than 3.

We present $F_{\rm evap}/F$ as a function of δ in Figure 9-C for different values of $N_{\rm evap}$. In the case of $N_{\rm evap}/N_{\rm low} < 1$ the effective $F_{\rm evap}$ is significantly reduced compared with the case of $N_{\rm evap}/N_{\rm low} > 1$.

In Figure 9-D we show $N_{\rm evap}$ as a function of $E_{\rm low}$ for different ratios $N_{\rm evap}/N_{\rm low}$. For $N_{\rm evap}$ located above the dotted curve in Figure 9-D, which corresponds to $N_{\rm evap}/N_{\rm low} = 1$, we have a weak dependence of $F_{\rm evap}$ from $N_{\rm evap}/N_{\rm low}$, which is shown in (Fig. 9-A and B). For $N_{\rm evap} > N_{\rm low}$ relative energy radiated by plasma above $N_{\rm evap}$ is determined by an expression $(F - F_{\rm evap})/F \propto (N_{\rm evap}/N_{\rm low})^{1-\delta/2}$ and one can conclude that $F_{\rm evap}$ for $\delta > 3$ mainly depends on the value of energy flux F carried by nonthermal electrons (Fig. 9-B).

Applying Equations (1) and (2) for fitting results presented in Table 1, we found the values of $F_{\rm evap}$ and $N_{\rm evap}$, which are summarized in Table 3 and Figure 10-A. We see that energetics of the chromospheric evaporation $F_{\rm evap}$ has the same order of magnitude for high-energy and low-energy flares, but $F_{\rm evap}$ of the low-energy flares is ∼2–3 times higher than $F_{\rm evap}$ of the high energy flares. The values of $N_{\rm evap}$ are very close to each other for all flares in the table when accounting for errors. The emission measure of the SXR emitting plasma is determined by the expression $EM = n^2V \sim N^2_{\rm evap}V/L^2 \propto N^2_{\rm evap}$. To connect the plasma temperature with the values of $F_{\rm evap}$ and $N_{\rm evap}$, one can use the energy balance equation assuming a dominant plasma heating by nonthermal electrons (without heat losses in the simplest case): $F_{\rm evap}\Delta tS \approx 3k_BT\sqrt{EMV} \sim 3k_BTN_{\rm evap}S$ and, thus, $T \propto F_{\rm evap}/N_{\rm evap}$. In Figure 10-B we show the values of $N^2_{\rm evap}$ and $F_{\rm evap}/N_{\rm evap}$ calculated for results presented in Table 2.

In Figure 10-C, $F_{\rm evap}/N_{\rm evap}$ and T (Table 1) are compared to each other. There is no positive correlation between these values, a fact that does not support our assumption $T \propto F_{\rm evap}/N_{\rm evap}$ and does not confirm temperature similarity of the studied flares. To estimate real flare temperatures we need additional physical modeling of energy balance in the flare region. Comparison between EM (Table 1) and $N^2_{\rm evap}$ is presented in Figure 10-D where we see a positive correlation between these values, a trend that supports our simplified analytical assumption $EM \propto N^2_{\rm evap}$. It is also remarkable that the values considering errors, the values of $N^2_{\rm evap}$ calculated for the studied flares do not differ from each other very much, which confirms similarity of the high-energy and low-energy flares.

Table 3 Comparison of the Calculated $F_{\rm evap}$ and $N_{\rm evap}$ for the Events from Table 1

Event date and UT	*GOES* class	$F_{\rm evap}$ (10^{10} erg cm^{-2} s^{-1})	$N_{\rm evap}$ (10^{20} cm^{-2})
25–Feb–2002, 02:56:40	M1.0	1.4±0.5	8.2±0.7
16–Apr–2002, 13:10:50	M2.5	4.6±1.3	10.7±0.8
11–Jul–2002, 14:17:55	M1.0	3.1±0.7	9.9±0.6
26–Feb–2002, 10:26:45	C9.6	5.2±5.5	10.3±4.5
28–Aug–2002, 10:59:30	C9.3	0.5±0.3	5.6±0.8
6–May–2005, 03:08:40	C5.7	1.5±1.3	7.4±2.2

According to the above analytical estimations and observational results, the spectral hardness of nonthermal electrons does not have a significant impact on efficiency of chromospheric evaporation in SXR emission. All distributions of flare thermal parameters have similar average values within one order of magnitude. It is more likely that intensity of chromospheric evaporation mostly depends on the total energy of nonthermal electrons injected into the dense atmosphere. To illustrate this, we present Figure 11, where we see a positive correlation ($r \approx 0.85$) between EM and $Fl(E > E_{\rm low})$ and a weak relationship ($r \approx 0.12$) between EM and δ. In this way, thermal similarity of two groups of flares is possible at approximately the same energy fluxes of nonthermal electrons. As $P_{\rm nth} \sim Fl(E > E_{\rm low})E_{\rm low}$, thus we have an approximately similar number of thermal electrons $n_{\rm nth}(E > E_{\rm low}) \propto Fl(E > E_{\rm low})/\sqrt{E_{\rm low}}$ involved in the acceleration process in the case of considered low-energy flares and high-energy flares.

The spatial analysis of the flare SXR sources that we performed with the *RHESSI* observations does not allow us to make precise conclusions about spatial structure of the flare sources. The fine structure of the flare region is very uncertain and to determine it we need a detailed comparison of ultraviolet and extreme ultraviolet images overlayed on *RHESSI* X-ray images synthesized by better imaging algorithms like PIXON. We also need more detailed numerical modeling, which could give more precise information about the thermal response of flare plasma to nonthermal electrons in different layers of the solar atmosphere.

7 CONCLUSIONS

We have selected two groups of flares with approximately similar X-ray classes but with different hardness of HXR spectra, and studied their observational peculiarities:

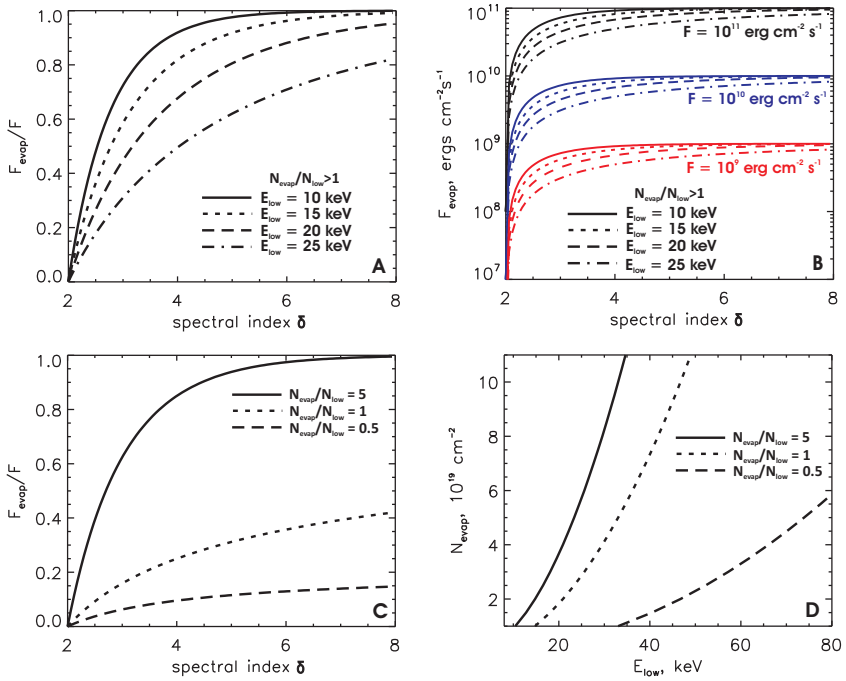

Fig. 9 Analytic calculations of the $F_{\rm evap}/F$ (panel A) and $F_{\rm evap}$ (panel B) for different low-energy cutoffs $E_{\rm low}$ and different energy fluxes F (panel B) according to Equation (2). Panel C presents $F_{\rm evap}/F$ calculated by Equation (2) for different values of $N_{\rm evap}/N_{\rm low}$. Panel D presents $N_{\rm evap}$ as a function of $E_{\rm low}$ for different ratios $N_{\rm evap}/N_{\rm low}$.

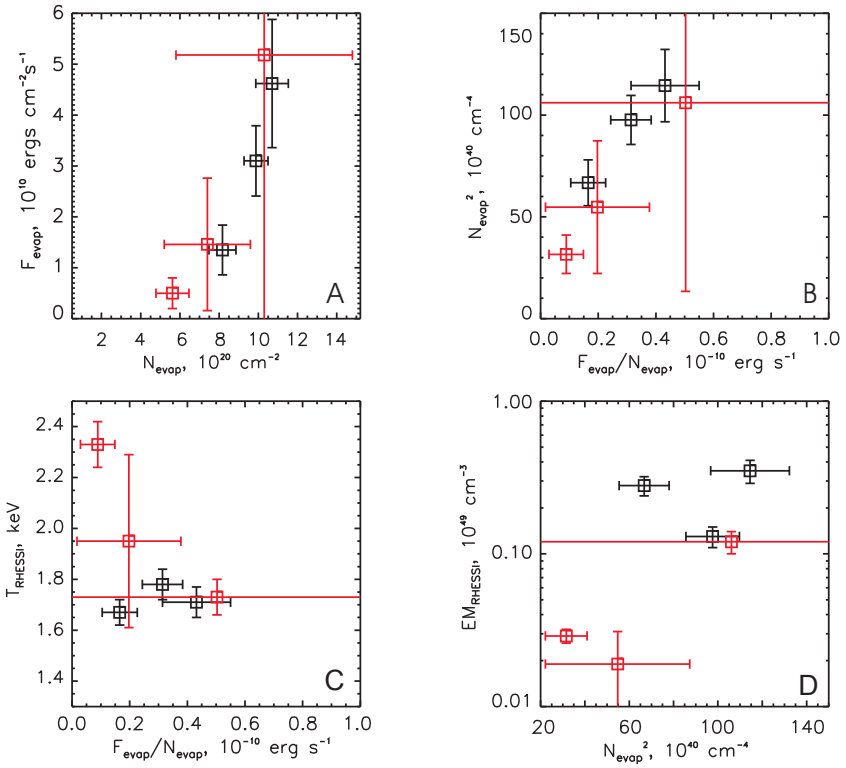

Fig. 10 Comparison of the events from Table 1: A) comparison of $F_{\rm evap}$ and $N_{\rm evap}$; B) comparison of $F_{\rm evap}/N_{\rm evap}$ and $N^2_{\rm evap}$; C) comparison of T obtained from fittings and $F_{\rm evap}/N_{\rm evap}$; D) comparison of EM obtained from fittings and $N^2_{\rm evap}$. Red and black correspond to the low-energy and high-energy flares respectively.

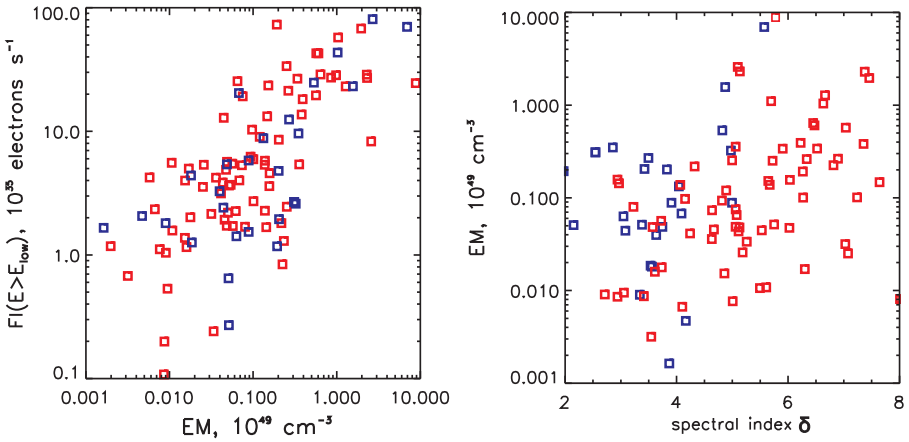

Fig. 11 The left panel shows total flux of the nonthermal electrons versus emission measure of the SXR emitting plasma. The right panel shows emission measure versus spectral index δ of nonthermal electron spectra. Red and blue correspond to the low-energy and high-energy flares respectively.

(1) Flares in the low-energy group (HXRs with energies less than 50 keV) have steep spectra of nonthermal electrons with a mean value of power law index $\delta \approx 5.8$, while flares in the high-energy group (HXRs with energies greater than 50 keV) have flatter spectra with $\delta \approx 3.9$. The case study analysis of six events shows a larger difference, in which the spectral indices are 6.9–7.5 for the low-energy group and 2.9–3.7 for the high-energy group.
(2) Flare thermal parameters (temperature, emission measure, Fe/Ni abundances, total radiated energy, SXR fluxes and rising time) derived from the *RHESSI* and *GOES* SXR observations for flares from these two groups do not show significant differences. Thus on average, events from the two groups show similar thermal properties.
(3) The sizes of the flare SXR sources are not statistically distinguishable between the two groups within the resolution capabilities of *RHESSI*.

Based on these observational results and analytical estimations, we conclude that different hardness of spectra of nonthermal electrons does not have a significant influence on the chromospheric evaporation. The total energy flux of nonthermal electrons is likely to play a major role in the efficiency of chromospheric evaporation and the resulting SXR fluxes. In this context, thermal similarity of events from two groups with different HXR hardness can be explained by means of approximately the same energy fluxes of nonthermal electrons heating the dense solar atmosphere. It leads to the consideration of a similar number of electrons involved in the acceleration process during low-energy and high-energy flares from similar *GOES* classes. To make a more precise investigation of peculiarities of flares, which are analogous to the event considered in this work, we need to consider more detailed spatially-resolved observations in different wavelengths and numerical modeling of the plasma response to nonthermal particles in flaring regions.

Acknowledgements The work is partly supported by RFBR projects 13-02-91165 and 15-32-21078. We are sincerely grateful to the hospitality provided by Purple Mountain Observatory in Nanjing (China), where part of the work was done, with grant support from MOST (973 program, 2011CB811402) and National Natural Science Foundation of China (11233008 and 11427803).

References

Battaglia, M., Grigis, P. C., & Benz, A. O. 2005, A&A, 439, 737
Bromund, K. R., McTiernan, J. M., & Kane, S. R. 1995, ApJ, 455, 733
Brown, J. C. 1971, Sol. Phys., 18, 489
Dennis, B. R., & Pernak, R. L. 2009, ApJ, 698, 2131
Dere, K. P., Landi, E., Young, P. R., et al. 2009, A&A, 498, 915
Emslie, A. G., Dennis, B. R., Shih, A. Y., et al. 2012, ApJ, 759, 71
Fisher, G. H., Canfield, R. C., & McClymont, A. N. 1985, ApJ, 289, 414
Fisher, G. H. 1989, ApJ, 346, 1019
Gan, W.-Q., Li, Y.-P., & Chang, J. 2001, ChJAA (Chin. J. Astron. Astrophys.), 1, 453
Guo, J., Liu, S., Fletcher, L., & Kontar, E. P. 2011, ApJ, 728, 4
Guo, J., Emslie, A. G., & Piana, M. 2013, ApJ, 766, 28
Hannah, I. G., Christe, S., Krucker, S., et al. 2008, ApJ, 677, 704
Hannah, I. G., Kontar, E. P., & Sirenko, O. K. 2009, ApJ, 707, L45
Hannah, I. G., Hudson, H. S., Battaglia, M., et al. 2011, Space Sci. Rev., 159, 263
Hurford, G. J., Schmahl, E. J., Schwartz, R. A., et al. 2002, Sol. Phys., 210, 61
Kontar, E. P., Dickson, E., & Kašparová, J. 2008, Sol. Phys., 252, 139
Krucker, S., & Lin, R. P. 2008, ApJ, 673, 1181
Li, Y. P., Gan, W. Q., & Feng, L. 2012, ApJ, 747, 133
Lin, R. P., Dennis, B. R., Hurford, G. J., et al. 2002, Sol. Phys., 210, 3

McDonald, L., Harra-Murnion, L. K., & Culhane, J. L. 1999, Sol. Phys., 185, 323
Neupert, W. M. 1968, ApJ, 153, L59
Ryan, D. F., Milligan, R. O., Gallagher, P. T., et al. 2012, ApJS, 202, 11
Saint-Hilaire, P., Krucker, S., & Lin, R. P. 2008, Sol. Phys., 250, 53
Sharykin, I. N., Struminskii, A. B., & Zimovets, I. V. 2015, Astronomy Letters, 41, 53
Smith, D. M., Lin, R. P., Turin, P., et al. 2002, Sol. Phys., 210, 33
Thomas, R. J., Crannell, C. J., & Starr, R. 1985, Sol. Phys., 95, 323
Veronig, A., Vršnak, B., Dennis, B. R., et al. 2002, A&A, 392, 699
Veronig, A. M., & Brown, J. C. 2004, ApJ, 603, L117
Xu, Y., Emslie, A. G., & Hurford, G. J. 2008, ApJ, 673, 576
Zimovets, I., & Struminsky, A. 2012, Sol. Phys., 281, 749